Colloid and Interface Science Communications 47 (2022) 100600

Contents lists available at ScienceDirect

Colloid and Interface Science Communications

journal homepage: www.elsevier.com/locate/colcom

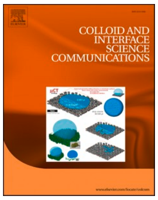

Rapid Communication

Shape stabilization and laser triggered shape transformation of magnetic particle functionalized liquid metal motors

Lin Wang [a], Sven Rutkowski [b,*], Tieyan Si [a,*], Tawheed Hashem [c], Bin Guo [a], Jie Xu [a], Anna I. Kozelskaya [b], Sergei I. Tverdokhlebov [b], Johannes Frueh [a,b,*]

[a] Key Laboratory of Microsystems and Microstructures Manufacturing, Ministry of Education, Mingde Building, Harbin Institute of Technology, XidaZhi Street 92, Harbin 150001, PR China
[b] Tomsk Polytechnic University, 634050, 30 Lenin Avenue, Tomsk, Russian Federation
[c] Institute of Functional Interfaces, Karlsruhe Institute of Technology, Hermann-von-Helmholtz-Platz 1, 76344 Eggenstein-Leopoldshafen, Germany

ARTICLE INFO

Keywords:
Liquid metal motor
Shape change
Polymeric shape stabilization
Magnetic control
Photothermal heating

ABSTRACT

Liquid metal motors made from biologically benign gallium are promising candidates for various applications ranging from drug delivery to targeting and killing cancer cells directly. One of the main problems with this novel technology is the need to utilize a membrane, making it possible to maintain a defined shape in order to perform the required functions. For magnetic remote guidance, liquid metal motors can be doped with magnetic iron microparticles, forming a transition magnetic liquid. In an alternative approach liquid metal structures are coated with magnetite nanoparticles. We hereby present an approach to laminate biologically benign gallium-based magnetic liquid metal motors with a biodegradable and biocompatible macromolecular thin film to retain the initial shape. Thanks to the polymer lamination and by the help of magnetic fields, the presented liquid metal motors can be remotely guided. The shape retaining macromolecular thin film can be liquefied by photothermal effects such as laser irradiation in order to change the shape of the liquid metal motor into a droplet due to surface energy minimization, allowing for penetration of structures smaller than the initial motor size. This work uses a relatively large technical demonstrator to show the technical realization and properties of this novel system, which opens up new paths and potential applications.

1. Introduction

Motion and enzymatic-controlled pumping are pivotal functions for higher forms of life [1,2]. For these reasons, the imitation of natural motors is one of the important fields of current research, with bio-artificial hybrid motors being the focus of ongoing research [3,4]. These artificial motors are promising candidates for fighting cancer and cardiovascular diseases by drug delivery [5,6]. In recent years, even wound sealing has become possible [5,6]. Other novel applications include nanoscopy and environmental remediation [5,7,8]. The research for these artificial micromotors began with investigating catalytic propulsion principles utilizing toxic fuels [9,10], followed by weak natural enzyme reactions for propelling [11,12] micro- and nanomotors [13], up to motors driven by magnetic and optical stimuli [14–16]. Recently, shape-changeable liquid metal motors propelled by acoustic fields have also been reported [17]. Such systems change optical properties on demand via shape changes [17]. In 2021, shape-changeable magnetic transformable liquid metal systems were reported that opened up entirely new application possibilities for this kind of material [18]. Remote-controlled and autonomous propelled liquid metal-based systems are a novel concept, and thus not yet fully understood. So far, solid metal motors have been driven by chemical reactions with stomach acid, increasing the pH level and delivering drugs, while solid-bound motors have been used to pump surrounding liquids depending on local pH, surrounding protein and surfactant conditions [19,20]. Liquid metal motors were in previous works reported to exhibit instabilities in shape, especially as the gallium oxide protective layer loses its effectiveness within a day (shape changes are visible within 30 min at pH = 5) [17]. For this reason, the greatest benefit of liquid metal motors, namely a controlled change in shape, has so far been severely limited.

An ideal liquid motor should be small enough to move inside the human body, can be remotely controlled, and exhibits stimulus-based shape changes. For example, maintaining the desired shape, while

---

* Corresponding authors.
E-mail addresses: rutkowski_s@tpu.ru (S. Rutkowski), tieyansi@hit.edu.cn (T. Si), Johannes.Frueh@hit.edu.cn (J. Frueh).

https://doi.org/10.1016/j.colcom.2022.100600
Received 23 August 2021; Received in revised form 1 February 2022; Accepted 2 February 2022
Available online 16 February 2022

moving and changing shape for defined tasks, or penetrating tissues based on controlled fragmentation of the delivery system as reported by De Geest [21,22]. The shapes and sizes required for the gastrointestinal system are larger than for the cardiovascular system, due to their different sizes, which allow objects up to cm in size [23].

This communication presents a proof-of-principle study for a biodegradable and biocompatible polymeric 3D structure preservation system. In the presented approach, a transition magnetic fluid (TMF) in liquid form is poured into a 3D printed mold, and the temperature is reduced until the TMF solidifies. After dissolving the mold, a polylactic acid (PLA) film is laminated onto the surface of the TMF, which enables the 3D motor shape to be retained even when the metal core inside is molten. The TMF motor can thus be guided in a magnetic field in both the liquid metal core and solid metal core state. Magnetic field-induced rotating and pulling motions are possible for remote guidance. Thermal destruction of the PLA layer allows for controlled shape changes of the liquid metal motor from helix and torpedo shape to round droplet shape. These changes in shape allow for thermal fusing a motor into thermoplastic surrounding structures like a petri dish. Furthermore, the volume reduction, as well as a simple disintegration of the TMF motor structure, aids the penetration of smaller structural features such as holes, since the motor fragments and reduced size are still magnetic.

2. Methods and materials

2.1. Synthesis of magnetite (Fe_3O_4) nanoparticles

Iron(II) chloride ($FeCl_2 \cdot 4\,H_2O$, m = 7 g, Tianjin Zhiyuan Chemical Reagent Co. Ltd., Tianjin, China) and Iron(III) chloride ($FeCl_3 \cdot 6\,H_2O$, m = 5.3 g, Tianjin Hengxing Chemical Reagent Manufacturing Co. Ltd., Tianjin, China) were dissolved in 200 mL ultrapure water (Purelab Classic from Elga Labwater, Lane End, High Wycombe, UK, resistance >18 mΩ × cm) to a yellow-colored solution while stirring with a magnetic stirrer (Jintan Xicheng Xinrui Instrument Factory, Changzhou, Jiangsu, P. R. China). An ammonia solution of 25 wt% (NH_4OH, purity: per analysis (P.A.), Tianjin Tianli Chemical Reagent Co. Ltd., Tianjin, P. R. China) was added dropwise until pH = 9 was reached. This starts the reaction for the magnetite production, which is visible, when the color changes from a yellow solution to a black dispersion. The dispersion was then stirred further for 30 min. After the reaction was complete, the generated Fe_3O_4 nanoparticles were collected with a rare earth permanent magnet, following the approach cited in reference [24]. All supernatant was decanted, and the particles were washed three times with ultrapure water. The Fe_3O_4 nanoparticles were freeze-dried (Beijing Bo Yi Kang Experimental Instrument Co. Ltd., Peking, P. R. China) and stored in powder form in a refrigerator at 4 °C.

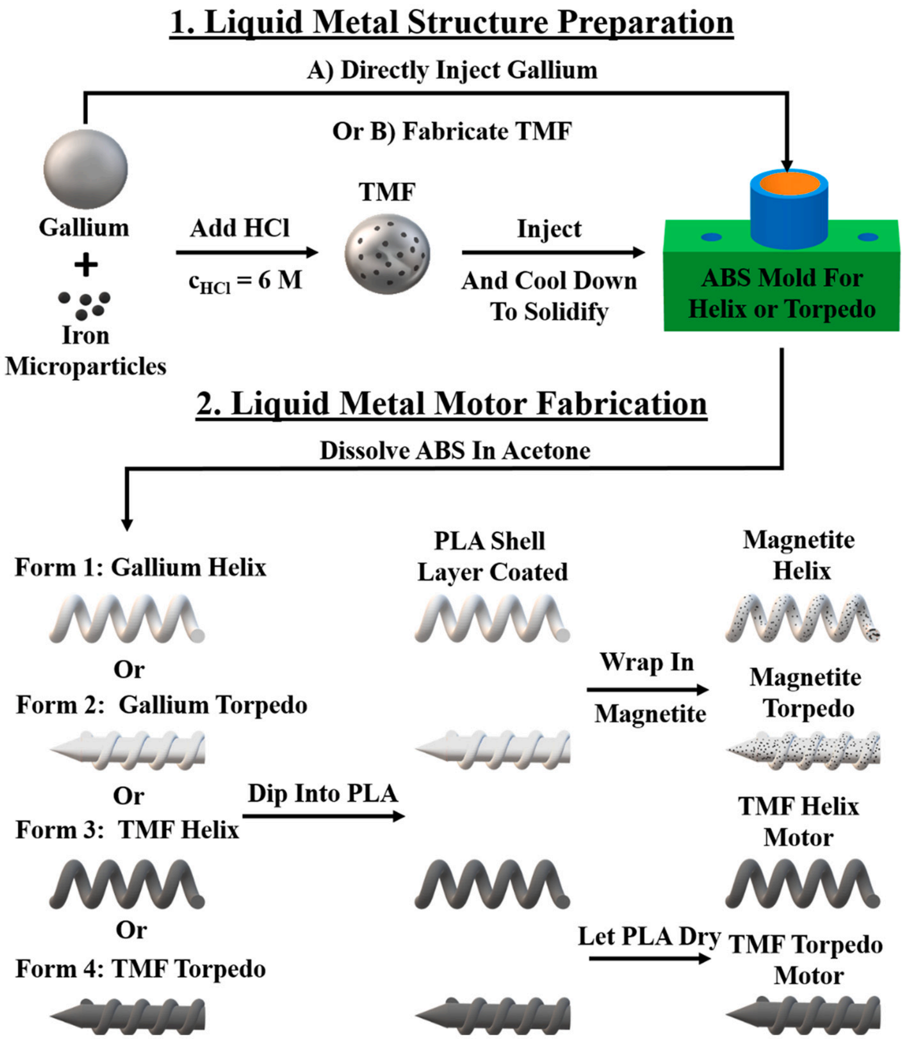

Fig. 1. Fabrication scheme of transition magnetic fluid (TMF) helix and torpedo motor, as well as the fabrication of magnetite coated gallium helix and torpedo motor. First part: liquid metal structure preparation over routine A) with the direct injection of gallium into the ABS mold or routine B) with the preparation of TMF and then the injection into the ABS mold. Second part: fabrication of TMF and gallium motors. Dissolving the ABS mold in acetone and afterwards, polylactic acid (PLA) shell layer coating (latter with subsequent magnetic functionalization). The gallium helix and torpedo structures are functionalized by enveloping magnetite (Fe_3O_4) nanoparticles for magnetic guidance.

2.2. Synthesis of transition magnetic fluid

First, 15 g of gallium (Dongguan Dingguan Metal Technology Co. Ltd., Dongguan, Guangdong, P. R. China) were placed in a 100 mL beaker in liquid form. Subsequently, 1 mL of 0.5% sodium hydroxide (NaOH, Tianjin Tianli Chemical Reagent Co. Ltd., Tianjin, P. R. China) was added in order to remove the gallium oxide layer on the gallium surface and to increase the flow behavior of the liquid metal. After this initial step, the NaOH was removed. In the following step, the gallium surface was covered with 1 g of iron microparticles (Fe, diameter: 38 μm, Nangong Xindun Alloy Welding Material Spraying Co. Ltd., Xingtai, Hebei, P. R. China). This step was followed by the addition of 10 mL of 6 mol/L hydrochloride acid (HCl, Tianjin Tianli Chemical Reagent Co. Ltd., Tianjin, P. R. China). At the same time, the solution was stirred until the free iron particles are either dissolved or dispersed in the gallium (no visible particles in the aqueous phase). A rare-earth permanent magnet (magnetic field strength: 350 mT) was employed to remove the generated magnetic fluid from the solution, and after solidification, to wash it five times with ultrapure water at room temperature (< 30 °C) to remove excess hydrochloric acid from the surface. It is worth noting that although iron has a higher density than gallium (7.8 g/cm^3 vs 5.9 g/cm^3). The similar surface energy that is minimized by stirring, causes the liquid gallium to flow around the iron microparticles at a high iron particle content. A high iron microparticle content is important to prevent iron particles to simply sink through the gallium to the bottom of the beaker, creating a gallium phase with and one without magnetic iron microparticles. Our approach allows the formation of transition magnetic fluid as discussed in detail in reference [18].

2.3. Preparation of Polylactic acid (PLA) solution

PLA at a mass of 3 g (3 mm nominal granule size, biopolymer, large molecular weight distribution, tradename Goodfellow 459–898-81, purchased via Merck KGaA, Darmstadt, Germany) was dissolved in 65.5 mL of chloroform ($CHCl_3$, Tianjin Tianli Chemical Reagent Co. Ltd., Tianjin, P. R. China) and stirred with a magnet stirrer (Jintan Xicheng Xinrui Instrument Factory, Changzhou, Jiangsu, P. R. China) until a clear solution was obtained.

2.4. 3D printing of the utilized molds

Microsoft 3D builder was utilized to draw the required 3D models on a standard PC with Windows 10 installed. These 3D models were converted via the enlightenment Cura software package (Enlightment, Wuhu, Anhui, China) to GCODE files for the 3D printer. A 3D printer (Version 3, Enlightment, Wuhu, Anhui, P. R. China) was utilized to print the required template. The 3D printer filament used was made from acrylonitrile butadiene styrene (ABS, Cixi Lanbo Printer Consumables Co. Ltd., Cixi City, Zhejiang, P. R. China) with a thickness of 1.75 mm, and the following printing parameters were used: nozzle diameter 0.4 mm, printing temperature 210 °C, heated bed temperature 30 °C, layer height 0.15 mm, shell thickness 0.8 mm, printing speed 40 mm/s. For the dimensions of 3D printed molds, see supporting information (SI) Fig. S1.

2.5. Preparation of magnetic helix-shaped motor

This shape was chosen because this and similar shapes allows corkscrew like swimming [25], which is of interest in a future extension of this work. Liquid metal gallium was injected into the 3D printed template (for template specifications see SI Fig. S1, for images of the injection process see SI Fig. S4) with a 1 mL syringe. After injection of the liquid metal, the filled template was placed into the refrigerator at 4 °C for solidification. Subsequently, the ABS template was dissolved in cold (4 °C) acetone (Tianjin Fuyu Fine Chemical Co. Ltd., Tianjin, P. R. China) to release the metal motors with defined shapes. The surface of the motor was covered with afore mentioned 3 wt% PLA solution by a single dip-coating step, which covers the motor with a PLA film of round about 2 μm, as described in reference [26]. It is worth mentioning that the PLA utilized has a wide range of molecular weights and the degradation rate of this polymer was reported to be in the timescale of days to weeks, depending on the pH of the surrounding solution [27] and highly on the polymer chain length [28]. For pure gallium motors in the shapes of helix and torpedo, superparamagnetic nanoparticles were adhered to the motor surface by rolling freshly fabricated gallium structures in PLA mixed with nanoparticle powder, followed by drying the sealing layer in air below the melting point of gallium. This step was repeated once to ensure that a significant number of magnetic nanoparticles were deposited on the surface to enable the magnetic guidance of the magnetized gallium motors (Fig. 1).

2.6. Preparation of magnetic torpedo-shaped motor

Warm water (> 35 °C) was utilized to melt the prepared magnetic fluid. This magnetic fluid was then filled into a 1 mL syringe. The total volume of 1 mL of liquid magnetic metal was injected with the syringe into the template, followed by dissolution of the template in cold (4 °C) acetone (Tianjin Fuyu Fine Chemical Co. Ltd., Tianjin, P. R. China) to release the motor. Similar to the helix motor, the torpedo motor was then laminated with a 3 wt% solution of PLA, and dried in air. Additionally, the gallium torpedo motor was magnetized analogously to the helix motor (Fig. 1).

2.7. Magnetic field strength vs. distance measurements

In order to determine the relationship between the magnetic field strength and the distance to a permanent magnet in one direction, two rulers were used, which were fixed parallel on one side of a rectangular permanent magnet. A Gauss meter (Senjie Technology Co. Ltd., Senjie Gaussmeter – SJ 200 Teslameter, Huizhou, Guangzhou, P. R. China) was used to determine the magnetic field strength at different distances along the channel formed by the two rulers. OriginPro 2019 (OriginLab Corporation, Northampton, Massachusetts, USA) was utilized to plot the data.

2.8. Movement of the motor within the magnetic field

The bottom side of a disposable petri dish was fixed on the Gauss probe of the SJ 200 Teslameter. Then the liquid metal motor was placed within the petri dish on the top of the measuring rod of the Gaussmeter and moved slowly in the direction of the permanent magnet along the rulers. A rare-earth magnet (magnetic field strength: 350 mT) was placed stationary at one end of the rulers. The distance where the magnetic motor started to move or to roll was recorded, as well as the value on the Gauss-meter. For rolling experiments, the motors were placed with their long axis perpendicular to the magnet field lines, and pulled parallel to the magnet field lines (Fig. 3D). The experiments were performed at 30–34 °C via a heated containment, and within a heated water bath to ensure the motors' liquid metal state, as the supplemental video S1 shows.

2.9. XRD characterization

The prepared magnetic fluid was dropped onto clean ice for solidification. Then the solidified magnetic fluid was collected and ground into powder for X-ray diffractometer (XRD) characterization by a PANalytical x'pert pro (PANalytical B.V., Almelo, Netherlands) in a scan range of 2θ from 5 to 90° within 5 min.

2.10. Zeta potential determination

A small amount of prepared magnetic fluid powder was dispersed in

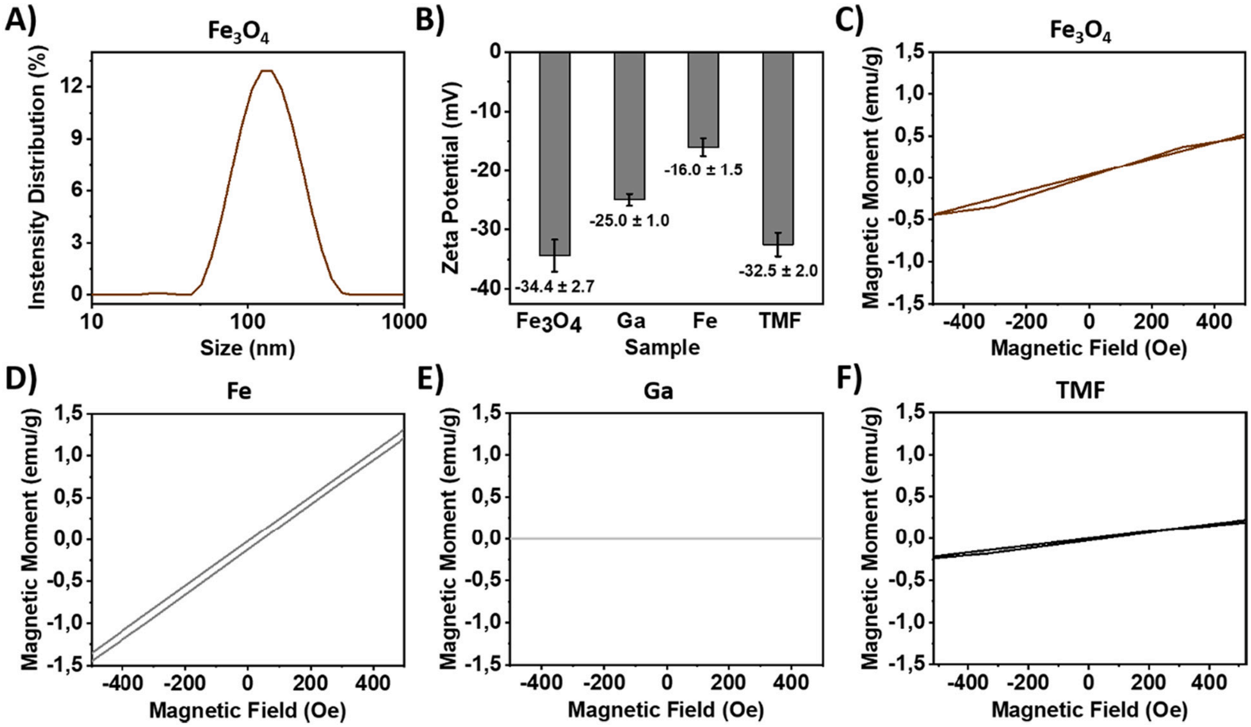

Fig. 2. Characterization of the investigated samples. A) Dynamic light scattering based size determination of magnetite (Fe_3O_4) nanoparticles, B) Zeta potential of the investigated samples; diagrams of the magnetic moments of C) paramagnetic magnetite (Fe_3O_4) nanoparticles; D) iron (Fe) microparticles; E) pure gallium (Ga) and F) transition magnetic fluid (TMF).

water by ultrasound (KQ-200KDE, Jiangsu Kunshan Ultrasonic Instrument Co. Ltd., Kunshan, Jiangsu, P. R. China) for ten minutes and followed by Zeta potential measurements with a Zeta potential analyzer (Malvern Nano-ZS90, Worcestershire, UK). The magnetite powder and the magnetic transition fluid were prepared and characterized analogous. For particle size characterization, the same Zeta potential analyzer was employed utilizing the following parameters: temperature: 25 °C, viscosity: 0.8872 cP, refractive index: 1.330, dielectric constant: 78.5, model: Smoluchowski, F(ka) value: 1.5, measurement duration: automatic (minimum 10 s – maximum 100 s, number of runs 11, run duration 10), analysis model: general-purpose (standard resolution).

2.11. Magnetic moment determination

For magnetic moment determination of the samples, dry powder of magnetite particles, magnetic transition fluid, iron microparticles, as well as pristine gallium was measured via a vibrating sample magnetometer at room temperature (model 7404, Lakeshore, Westerville, Ohio, USA) ranging from - 15,000 OE to +15,000 OE.

2.12. Laser irradiation and stimulated shape changes

Two different lasers were utilized for these experiments. Both are C-type multimode diode lasers (purchased from FS-Optics, Shanghai, P. R. China) with the difference that the first laser works with 2 W power and a wavelength of 808 nm and the second laser works with 5 W and a wavelength of 950 nm. Both lasers operate in the continuous wave mode and utilize manual power control units (ATR-1800, FS-Optics Optics, Shanghai, P. R. China). The photothermal heating by direct irradiation of the samples was achieved using a laser without additional focusing at 0.5–2.5 cm distance. The beam shape is due to the C-type diode oval (aspect ratio ~ 1: 2), with a laser spot diameter of ~2.5 × 1.25 mm.

2.13. Calculation of magnetic properties and magnetic work of the liquid metal motors

For determining the work performed by the liquid metal motors, the magnetic field of the utilized permanent magnet was first determined and then the magnetic field gradient was calculated. In a further step, the volume and weight of the motors were determined. Subsequently, the motors were lifted from a petri dish in air environment, as well as being submerged in hot and cold water. The lifting was performed by a rare earth permanent magnet. In this way, the necessary field gradients to move the motors within respective environments and the work were determined, which these motors can perform, without experiencing uncertainties from the unknown surface roughness of the motors in terms of friction losses. Utilizing the determined work, motion angle and travelled distance relation, the torque ($\gamma = \nu \times F$, with F being the force and ν the travelling vector) was determined followed by a calculation of the magnetic moment μ via the relationship $\mu = \gamma/H$, with H being the magnetic field strength. The magnetization was determined by the relationship $M = \mu/V$, with V being the volume of the motors. The magnetic susceptibility χ of the motors was calculated according to $\chi = M/H$. The produced magnetically induced force of the motors was calculated via two different equations, one taking the product of the magnetic field and field gradient into account ($F = \chi \times m \times H \times \Delta H$) and a simplified equation ($F = \Delta(\chi \times H)$), with ΔH being the field gradient and m the mass. All equations in this section were obtained from reference [29].

3. Results and discussion

In air, pristine gallium forms an oxide layer on its surface within minutes, which effectively prevents molten gallium from flowing below the surface (supporting information (SI) Fig. S2A) [18,30]. This oxide layer must be etched away with diluted sodium hydroxide solution (SI Fig. S2B) in order to be able to process the gallium further [18,30]. The incorporation of magnetic iron microparticles is necessary to enable

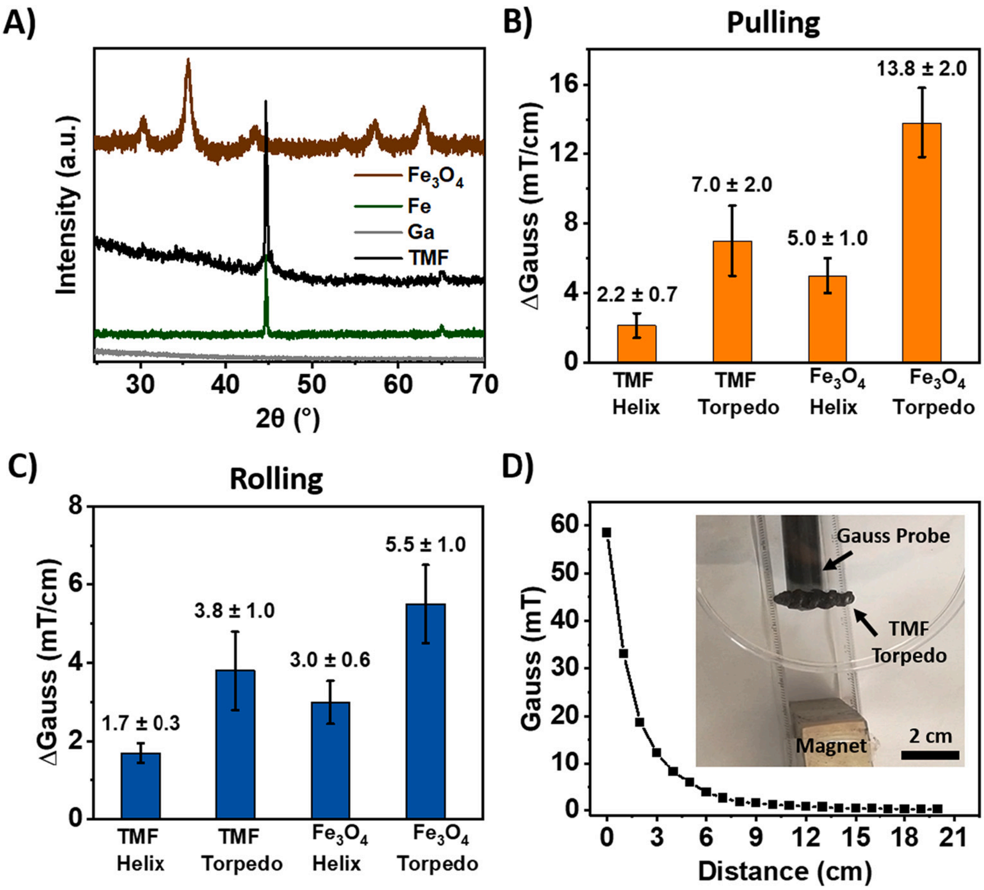

Fig. 3. Characterization of motors based on liquid metal. A) X-ray diffraction (XRD) of magnetite nanoparticles (Fe_3O_4), iron microparticles (Fe), gallium (Ga), and transition magnetic fluid (TMF). B) Magnetic field strength gradients required for pulling liquid metal motors in the direction of a magnet; C) Magnetic field strength gradients required to induce a rolling movement of liquid metal motors; D) Distance vs. magnetic field strength, which displays a strong gradient (for calculated gradient see SI Fig. S6) inset displays a photograph of the experimental setup with Gauss probe, magnet and magnetite coated gallium liquid metal motor in the utilized torpedo shape.

remote guidance. Successful integration of iron-metal microparticles was achieved utilizing the approach of reference [18] (Fig. 1). This allows the creation of a transitional magnetic fluid (TMF), which, due to its inherent magnetic force, can hold its own weight, but also macroscopic objects against gravity (Fig. 1, SI Fig. S3).

After the virtual structures for the liquid metal motor-based templates were designed on a PC, they were 3D-printed with acrylonitrile butadiene styrene (ABS). This 3D printed template allows for injection of the liquid TMF for mold-based structure creation and releases after the mold was dissolved in cold acetone (4 °C) (Fig. 1A, B and SI Fig. S1, S4). Since liquid metal is unable to retain the template structure by itself, it is mandatory to dissolve the 3D-printed ABS mold in acetone at a temperature below the TMF melting point. This is followed by lamination using polylactic acid (PLA) because the glass transition temperature of PLA is higher than the melting point of gallium (> 60 °C vs. 29 °C). A pure gallium helix was functionalized with magnetite (Fe_3O_4) nanoparticles incorporated within the PLA lamination layer to determine the most efficient magnetic particle placement and guidance efficiency.

The paramagnetic nanoparticles produced have an average size of ~100 nm, with a zeta potential of $\zeta \approx -35\ mV$ (Fig. 2A and B). Both gallium ($\zeta = -25\ mV$) and pristine iron microparticles ($\zeta = -16\ mV$, obtained from reference [30]) offer a lower zeta potential, which is significantly lower than that of the TMF ($\zeta = -32\ mV$). Magnetite and TMF have similar zeta potential values (Fig. 2B).

The determination of the magnetic moment of different samples shows that the magnetic properties of the iron microparticles are higher than the one of paramagnetic magnetite particles (Fig. 2D vs. Fig. 2F). Furthermore, iron microparticles containing samples display a larger hysteresis (area within the magnetization curve) compared to paramagnetic magnetite nanoparticles (Fig. 2D vs. Fig. 2F), which is a common difference between ferromagnetic and paramagnetic materials.

As expected, pure gallium shows no magnetic properties (Fig. 2E). The strong magnetization as well as the significant hysteresis of the TMF proves the successful incorporation of ferromagnetic iron microparticles into gallium (Fig. 2F). X-ray diffraction measurements reveal clear differences between these systems (Fig. 3A), proving the successful incorporation of iron microparticles. This result is confirmed by EDX measurements proving the presence of iron within the TMF, as demonstrated in SI Fig. S5. It is worth mentioning that this incorporation of iron into TMF is possible despite differences in density between Ga and Fe (5.9 g/cm^3 vs. 7.8 g/cm^3) due to similar surface energy of both metals and the resulting minimization of the surface force. In addition, a high amount of utilized iron microparticles was present in the TMF (~ 26 wt% of the final tested motors, due to the collection of TMF from the lower portion of the bottom of the beaker). Analyzing the motor compositions by X-ray diffraction, different peak positions between magnetite nanoparticles, gallium and iron are evident (Fig. 3A).

Since the XRD spectra of iron and TMF display the same peak (at 2θ ≈ 45°), the successful incorporation of iron microparticles into gallium to form TMF has been proven (Fig. 3A). TMF employs not only a larger amount of magnetic material (3–10 times, depending on utilized motor shape) but also significantly stronger ferromagnetic iron microparticles compared to paramagnetic magnetite nanoparticles on top of the gallium motors (for a more detailed analysis of magnetic properties see lower sections). An anisotropic magnetite nanoparticle placement within the PLA sealing layer on the TMF as well as the pure gallium helices (SI Fig. S7) is achieved by dipping the motors manually with an undried PLA sealing layer into magnetite nanoparticle powder. As with a homogeneous magnetite nanoparticle distribution over the entire surface, this type of particle placement also enables a remote-controlled spiral movement within a 3D magnetic guidance setup in aqueous environments (SI videos S2 and S3). There is no improvement in the motor

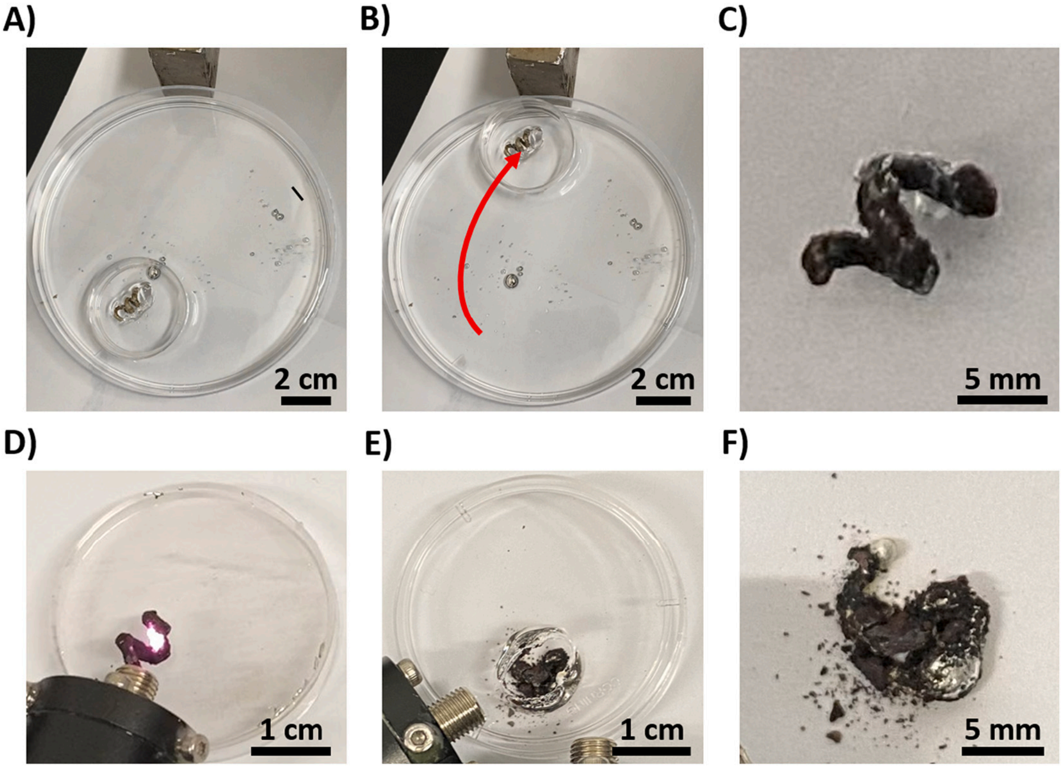

Fig. 4. Laser-based photothermal effects of transition magnetic fluid (TMF) and magnetized gallium motors: A) TMF helix motor, which was due to photothermal effects integrated into a petri dish boat and B) same as A) being attracted by a magnet (the red arrow indicates the motion path). C) Magnetite-coated gallium helix motor; D) laser-exposed magnetite-coated gallium helix motor; E) shape-changed gallium helix motor after 3.5 min of laser exposure melting it through a polystyrene petri dish; F) zoom at molten and shape-changed magnetite-coated gallium helix motor. Utilized lasers were a 2 W and 808 nm laser together with 5 W and 950 nm laser; exposure time was 3.5 min for both lasers. (For interpretation of the references to color in this figure legend, the reader is referred to the web version of this article.)

guidance in the case of anisotropic magnetite nanoparticle placement, neither for the gallium nor for the TMF motor. Therefore, this test was only performed on helix motor shapes and experiments with homogeneous magnetite distribution were continued on gallium motors and pure TMF motors.

Pulling the torpedo-shaped motors over the surface requires for both types of motor compositions significantly higher magnetic field gradients compared to the helix-shaped motor (Fig. 3B). This finding is surprising, as the TMF helix and torpedo motors should respond based on their composition similar to the magnetic field gradient. We explain this observation with the frictional forces that the motors experience on the petri dish surface, as pulling causes the motors to experience frictional forces. The torpedo-shaped motors are in both cases significantly heavier than the helix-shaped motors; therefore, the surface friction forces are higher. Friction forces however cannot be utilized to explain the observed higher requirement in magnetic field gradient to rotate the torpedo-shaped motors compared to the helix-shaped motors (Fig. 3C). This observation is explained with the rough printing structure, which causes rough surfaces (printing errors are determined by microscopic images to be within in a range between 50 and 100 μm). Therefore, weight-dependent energy losses also occur in motion, similar to friction, in simple rolling and pulling experiments as displayed in Fig. 3B and C. As discussed above, the surface bound friction and roughness effects have an adverse effect on the measurements of the magnetic field strength required to move the liquid metal motors, thus these contributions should be minimized or eliminated.

For these reasons, pulling experiments of the motors against gravity in air and aqueous environments were performed, for more details see SI Fig. S8. In this figure it can be seen that the distance between the rare earth magnet and the motors were decreased until the motor begun to be lifted up and thus required magnetic field gradient is highly depending on the internal composition and in case of the magnetite coated motors from the surface to volume ratio (SI Fig. S9). For the homogeneous and surface to volume composition independent TMF motors, the required magnetic field gradient is shape independent. The resultant work performed by the motors is however based on the motor weight, and travelled distance, thus the highest work is performed by the TMF torpedo-shaped motor, followed by the TMF and magnetite helix-shaped motors (SI Fig. S9D). Due to this difference in mass and thus different applied magnetic materials, the resultant torque (SI Fig. S10A) is also differing for each type of liquid metal motor. This results in a magnetic material dependent magnetic moment (SI Fig. S10B), motor magnetization (SI Fig. S10C) and thus magnetic susceptibility (SI Fig. S10D). The force exerted by the motors is highest for the TMF based motors, due to highest magnetic susceptibility and magnetic moment. Torpedo-shaped motor coated with magnetite exerts orders of magnitude lower force (~ 10^{-3} compared to 10^{-6}), due to the lowest surface to volume ratio and thus lowest relative amount of magnetic material (SI Fig. S11). It is worth noting that the differences in the work performed by the TMF helix and the TMF torpedo-shaped motor can be explained simply by the factor of the mass differences between these two liquid metal motors. The differences of produced force for the magnetite-based motors differ depending on the utilized equation within 1 to 1.5 orders of magnitude and is dependent on the surface to volume ratio between magnetite and gallium. In case of the magnetite coated torpedo-shaped motors, the more precise equation relating to the product of magnetic field amplitude and the field gradient causes a significant under-estimation of the produced force, due to the generally relatively low magnetic susceptibility of the motor (SI Fig. S11A vs. S11B). Regarding magnetic performance and work within differing environments and media, SI Fig. S9 – S11 display differences for air, hot and cold water for all tested samples, whereby TMF motors display a slight increase in warm water compared

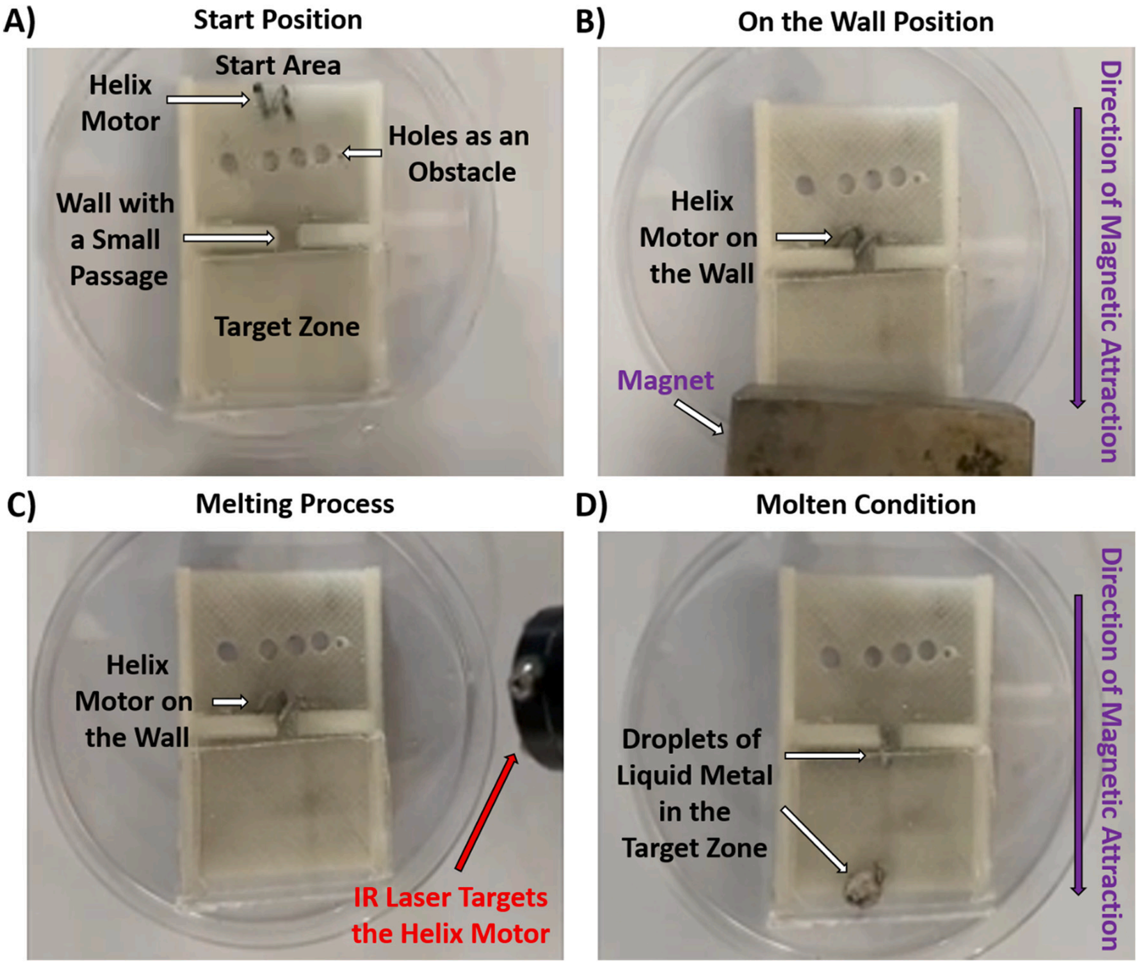

Fig. 5. Solving an obstacle course utilizing a helix-shaped TMF motor sealed with a PLA layer. A) Start position, B) motor touching a wall with a passage smaller as the size of the motor, C) Motor irradiated by an IR laser with 5 W power and a wavelength of 950 nm, D) motor penetrating the hindrance wall in molten and fragmented condition. The photographs are taken from the SI video S5.

to decrease in cold water. This difference can be attributed to the reduced viscosity for warm water, and the contrary increased viscosity for cold water (1.3 cP at 10 °C and 0.79 cP at 30 °C), which was due to omission of surface friction not corrected for in the presented experiments. The diminished performance of the magnetite coated torpedo-shaped motor and slight decrease in performance of the magnetite coated helix-shaped motor is related to the temperature-induced reduction of magnetic susceptibility for paramagnetic particles [31].

The observed finding of a lower required magnetic field gradient for the TMF motors in all kinds of experiments is explained with the higher iron content compared to the amount of paramagnetic magnetite particles (12 ± 5% vs. 3 ± 2%). Furthermore, stronger magnetic susceptibility of iron microparticles (8χ), which offer a bulk ferromagnetic magnetism compared to paramagnetic nanoparticles which offer a magnetic susceptibility of $\sim 0.0067\chi$ that leads to a higher magnetization of the iron particles (difference in magnetic susceptibility ~ 1164) [32,33].

Exposing empty Petri dishes to laser irradiation did not show any material changes and only a slight increase in the local temperature at full laser power for 5 min from either the 808 nm, 950 nm or even both laser at the same time (SI Fig. S12). The laser exposure of the utilized liquid metal structures causes significant local photothermal heat generation, especially on metallic surfaces [34,35]. It should be noted that the heating rates for the non-focused laser with a power of 2 W and a wavelength of 808 nm is surpassing the PLA glass transition temperature (SI Fig. S13). Using a stronger laser with 5 W power and 950 nm wavelength allows achieving even higher temperatures (SI Fig. S13). Moreover, by combining both lasers, the PLA surface layer can also be softened enough outside of the directly irradiated area within less than two minutes, to allow for disintegration of the complete motor shape (SI Fig. S13, S14). The time required to soften the PLA layer without the 808 nm wavelength laser increases the PLA sealing layer opening time up to three minutes. It is especially worth mentioning, that laser-generated heat can reach locally up to $>>300$ °C within the nanometer range [36], whereby up to 7000 K temperature increase are theoretically possible for metallic 200 nm particles in the focus of optical traps in air [37]. In contrast, in the micrometer range, polymeric melting temperatures are surpassed easily and reports from others even describe fire-like effects [6,36]. These local temperature measurements prove that on local scale the conditions of polymeric melting are fulfilled, as the sealing and shape retaining polymer layer of the PLA utilized is in the range of several hundred nanometers up to one micrometer, as pointed out in an earlier work [38]. We can therefore assume that at least within the direct laser irradiated area the PLA layer is in liquid state, while outside of this area it is significantly softened by surpassing the glass-transition temperature T_g. Additionally, this significant increase in temperature was confirmed in this study by thermal IR measurements of a helix-shaped motor (SI Fig. S13), and the presence of molten polymer petri dishes (Fig. 4). A TMF helix-shaped motor placed into a petri dish was guided to the desired position and anchored stably through thermal polymer fusion with the petri dish into this position. This stable anchoring allows using the magnetic properties of TMF as a boat motor within the petri dish in aqueous environments (Fig. 4A and B). SI video S4 displays a smaller petri with a TMF helix motor inside employed as a dish boat in a bigger petri dish filled with water being attracted by a magnet.

The increase in laser power and irradiation time allows complete melting of the covering PLA polymer film, which leads to a total structural loss of the liquid metal motor (Fig. 4C – F). It is worth noting that achieved temperatures are high enough to completely disintegrate a polymeric petri dish by melting a motor through a polystyrene petri dish (Fig. 4C – F). Since the melting temperature of polystyrene is 270 °C, the efficiency of the used approach is emphasized. The potential applications are manifold, even shape modifying or relatively high-melting thermoplastic polymers can be utilized as the sealing layer of the liquid metal motors.

Successful photothermal heating and shape-changing of the liquid metal core by melting the sealing polymer layers were confirmed for all investigated structures (SI Fig. S14 – S16). Observed shape change did not cause any increase or decrease in photothermal heating, as the laser spot size is smaller than motor frame parts or the final droplet. The torpedo-shaped motor, despite the previous leakage of the liquid metal, requires a magnetic attraction in order to dismantle its shape completely (SI Fig. S16). This effect is most likely due to the existing lower surface to volume ratio of the torpedo-shaped motor.

In order to demonstrate the potential of the changeable shape system, a TMF motor was used to complete an obstacle course. Fig. 5 displays photographs that describe the process and the experimental layout of the obstacle course; these photographs are taken from SI video S5. This obstacle course contains holes at the bottom of the path, which would cause a liquid metal motor without a sealing layer to flow through the holes, while the wall with a small passage in front of the target zone requires a liquid metal motor with released liquid metal to reach the goal. This experiment demonstrates the potential of liquid metal motors. In the experiment performed, a helix-shaped TMF motor completes the obstacle course and reaches the goal in a shape-modified and fragmented manner (Fig. 5 and SI video S5). Such a fragmentation is beneficial, as stated out in the work from De Geest et al., in which triggered fragmenting drug delivery systems and fragmentation-based drug release were demonstrated [21,22,39]. Inspired by De Geest we intend to improve the presented work in the future by turning a large liquid metal motor into many smaller motors for defined technical tasks or drug delivery applications. The presented demonstrator opens therefore new ways for utilizing liquid metal systems.

4. Conclusions

In this communication, we reported a method of employing a biocompatible and biodegradable macromolecular membrane to stabilize the shape of a magnetic motor based on liquid metal. The utilized liquid metal motors can be functionalized with magnetic particles in two ways: firstly by incorporating iron microparticles into the liquid metal core (transition magnetic fluid), which enables a magnetic transition liquid metal system, and secondly by incorporating paramagnetic nanoparticles into the shape-retaining polymeric surface membrane. Both ways enable controlled magnetic guidance and motion of the motors. The magnetic transition fluid enables a stronger magnetic susceptibility and thus requires up to factor of two lower magnetic field gradients for control compared to functionalization with magnetite nanoparticles within the shape-stabilizing PLA sealing layer. Anisotropic distribution of paramagnetic nanoparticles on transition magnetic fluid and gallium motors allows for remote control of helix-shaped motors within 3D magnetic guidance systems. A laser-induced sealing layer liquefaction allows triggered changes in the shape of the motor, whereby the magnetic liquid metal motors can be incorporated into different polymeric structures trough considerable heating, in order to function as motors within them. A triggered shape and size reduction due to the disintegration of the polymeric shell layer is not fully controllable, as either a droplet can be formed, or a fragmentation of the liquid metal motor can occur, as it was shown by a solved obstacle course. In this solved obstacle course, laser was irradiating without additional focusing on one side of the liquid metal motor, to allow for PLA sealing layer liquefaction. The work presented here is a basis for future miniaturization of liquid metal motors utilizing helical shapes for corkscrew-like swimming within oscillating magnetic fields.

CRediT authorship contribution statement

Lin Wang: Investigation. **Sven Rutkowski:** Data curation, Visualization, Writing – review & editing. **Tieyan Si:** Data curation, Formal analyis. **Tawheed Hashem:** Resources. **Bin Guo:** Supervision. **Jie Xu:** Supervision. **Anna I. Kozelskaya:** Writing – review & editing. **Sergei I. Tverdokhlebov:** Supervision, Funding acquisition. **Johannes Frueh:** Writing – original draft, Writing – review & editing, Conceptualization, Project administration.

Declaration of Competing Interest

The authors declare no conflict of interest.

Acknowledgements

This research was supported by National Natural Science foundation of China, (Grant No.: 22172043) (J.F.). This research was supported by the TPU development program.

Appendix B. Supplementary data

Supporting Information contains video S1, which shows the cutting of a motor PLA sealing layer with liquid metal flowing out, videos S2 - S3 display moving motors in aqueous conditions, video S4 displays a motor welded into a polymer petri dish and being used to guide the petri dish like a motorboat on water, the supporting files further contain schemes of the production of liquid metal motors, an experimental scheme, diagrams of the magnetic properties of the liquid metal motors, photographs of the forms, and production as well as photographs of the liquid metal motors during laser exposure.

References

[1] O.E. Shklyaev, H. Shum, A. Sen, A.C. Balazs, Harnessing surface-bound enzymatic reactions to organize microcapsules in solution, Sci. Adv. 2 (2016), e1501835, https://doi.org/10.1126/sciadv.1501835.

[2] D. Walker, B.T. Käsdorf, H. Jeong, O. Lieleg, P. Fischer, Enzymatically active biomimetic micropropellers for the penetration of mucin gels, Sci. Adv. 1 (2015) 33–35, https://doi.org/10.1126/sciadv.1500501.

[3] J. Simmchen, J. Katuri, W.E. Uspal, M.N. Popescu, M. Tasinkevych, S. Sánchez, Topographical pathways guide chemical microswimmers, Nat. Commun. 7 (2016) 10598, https://doi.org/10.1038/ncomms10598.

[4] V. Magdanz, I.S.M. Khalil, J. Simmchen, G.P. Furtado, S. Mohanty, J. Gebauer, H. Xu, A. Klingner, A. Aziz, M. Medina-Sánchez, O.G. Schmidt, S. Misra, IRONSperm: Sperm-templated soft magnetic microrobots, Sci. Adv. 6 (2020) eaba5855, https://doi.org/10.1126/sciadv.aba5855.

[5] B. Wang, K. Kostarelos, B.J. Nelson, L. Zhang, Trends in micro-/nanorobotics: materials development, actuation, localization, and system integration for biomedical applications, Adv. Mater. 33 (2021) 1–44, https://doi.org/10.1002/adma.202002047.

[6] W. He, J. Frueh, N. Hu, L. Liu, M. Gai, Q. He, Guidable thermophoretic janus micromotors containing gold nanocolorifiers for infrared laser assisted tissue welding, Adv. Sci. 3 (2016) 1600206, https://doi.org/10.1002/advs.201600206.

[7] J. Li, W. Liu, T. Li, I. Rozen, J. Zhao, B. Bahari, B. Kante, J. Wang, Swimming microrobot optical nanoscopy, Nano Lett. 16 (2016) 6604–6609, https://doi.org/10.1021/acs.nanolett.6b03303.

[8] W. Gao, X. Feng, A. Pei, Y. Gu, J. Li, J. Wang, Seawater-driven magnesium based Janus micromotors for environmental remediation, Nanoscale. 5 (2013) 4696–4700, https://doi.org/10.1039/c3nr01458d.

[9] R.F. Ismagilov, A. Schwartz, N. Bowden, G.M. Whitesides, Autonomous movement and self-assembly, Angew. Chem. Int. Ed. 41 (2002) 652–654, https://doi.org/10.1002/1521-3773(20020215)41:4<652::AID-ANIE652>3.0.CO;2-U.

[10] W. Gao, S. Sattayasamitsathit, J. Orozco, J. Wang, Efficient bubble propulsion of polymer-based microengines in real-life environments, Nanoscale. 5 (2013) 8909–8914, https://doi.org/10.1039/c3nr03254j.

[11] M. Xuan, J. Li, Photosystem II-based biomimetic assembly for enhanced photosynthesis, Natl. Sci. Rev. (2021), https://doi.org/10.1093/nsr/nwab051.

[12] Y. Jia, M. Xuan, X. Feng, L. Duan, J. Li, J. Li, Reconstitution of motor proteins through molecular assembly, Chin. J. Chem. 38 (2020) 123–129, https://doi.org/10.1002/cjoc.201900382.

[13] S. Cao, J. Shao, H. Wu, S. Song, M.T. De Martino, I.A.B. Pijpers, H. Friedrich, L.K.E. A. Abdelmohsen, D.S. Williams, J.C.M. van Hest, Photoactivated nanomotors via aggregation induced emission for enhanced phototherapy, Nat. Commun. 12 (2021), https://doi.org/10.1038/s41467-021-22279-w.

[14] X.-Z. Chen, N. Shamsudhin, M. Hoop, R. Pieters, E. Siringil, M.S. Sakar, B.J. Nelson, S. Pané, Magnetoelectric micromachines with wirelessly controlled navigation and functionality, Mater. Horiz. 3 (2016) 113–118, https://doi.org/10.1039/C5MH00259A.

[15] S. Sengupta, M.M. Spiering, K.K. Dey, W. Duan, D. Patra, P.J. Butler, R. D. Astumian, S.J. Benkovic, A. Sen, DNA polymerase as a molecular motor and pump, ACS Nano 8 (2014) 2410–2418, https://doi.org/10.1021/nn405963x.

[16] A.P. Bregulla, H. Yang, F. Cichos, Stochastic localization of microswimmers by photon nudging, ACS Nano 8 (2014) 6542–6550, https://doi.org/10.1021/nn501568e.

[17] D. Wang, C. Gao, W. Wang, M. Sun, B. Guo, H. Xie, Q. He, Shape-transformable, fusible rodlike swimming liquid metal nanomachine, ACS Nano (2018), https://doi.org/10.1021/acsnano.8b05203.

[18] H. Wang, S. Chen, H. Li, X. Chen, J. Cheng, Y. Shao, C. Zhang, J. Zhang, L. Fan, H. Chang, R. Guo, X. Wang, N. Li, L. Hu, Y. Wei, J. Liu, A liquid gripper based on phase transitional metallic ferrofluid, Adv. Funct. Mater. 2100274 (2021) 2100274, https://doi.org/10.1002/adfm.202100274.

[19] J. Li, S. Thamphiwatana, W. Liu, B. Esteban-Fernández de Ávila, P. Angsantikul, E. Sandraz, J. Wang, T. Xu, F. Soto, V. Ramez, X. Wang, W. Gao, L. Zhang, J. Wang, Enteric micromotor can selectively position and spontaneously propel in the gastrointestinal tract, ACS Nano 10 (2016) 9536–9542, https://doi.org/10.1021/acsnano.6b04795.

[20] Z. Zhao, Z. Wu, S. Rutkowski, S.I. Tverdokhlebov, J. Frueh, Influence of the pH value and the surfactant concentration on the pumping performance of magnesium fuel based Janus micropumps, Colloids Surfaces A Physicochem. Eng. Asp. 626 (2021), 127081, https://doi.org/10.1016/j.colsurfa.2021.127081.

[21] B.G. De Geest, S. De Koker, J. Demeester, S.C. De Smedt, W.E. Hennink, Self-exploding capsules, Polym. Chem. 1 (2010) 137, https://doi.org/10.1039/b9py00287a.

[22] B.G. De Geest, N.N. Sanders, G.B. Sukhorukov, J. Demeester, S.C. De Smedt, Release mechanisms for polyelectrolyte capsules, Chem. Soc. Rev. 36 (2007) 636–649, https://doi.org/10.1039/B600460C.

[23] J. Li, P. Angsantikul, W. Liu, B. Esteban-Fernández de Ávila, S. Thamphiwatana, M. Xu, E. Sandraz, X. Wang, J. Delezuk, W. Gao, L. Zhang, J. Wang, Micromotors spontaneously neutralize gastric acid for pH-responsive payload release, Angew. Chem. 129 (2017) 2188–2193, https://doi.org/10.1002/ange.201611774.

[24] D.A. Gorin, S.A. Portnov, O.A. Inozemtseva, Z. Luklinska, A.M. Yashchenok, A. M. Pavlov, A.G. Skirtach, H. Möhwald, G.B. Sukhorukov, Magnetic/gold nanoparticle functionalized biocompatible microcapsules with sensitivity to laser irradiation, PCCP. 10 (2008) 6899–6905, https://doi.org/10.1039/b809696a.

[25] L. Dong, L. Zhang, M. Yu, B.J. Nelson, Nanorobotic manipulation of helical structures, in: Y. Sun, X. Li (Eds.), Micro- and Nanomanipulation Tools, 1st ed, Wiley VCH, Weinheim, 2015, pp. 477–485, https://doi.org/10.1002/9783527690237.

[26] M. Gai, J. Frueh, T. Tao, A.V. Petrov, V.V. Petrov, E.V. Shesterikov, S. I. Tverdokhlebov, G.B. Sukhorukov, Polylactic acid nano- and microchamber arrays for encapsulation of small hydrophilic molecules featuring drug release via high intensity focused ultrasound, Nanoscale. 9 (2017) 7063–7070, https://doi.org/10.1039/C7NR01841J.

[27] Y. Liu, M. Gai, D. Sukvanitvichai, J. Frueh, G.B. Sukhorukov, pH dependent degradation properties of lactide based 3D microchamber arrays for sustained cargo release, Colloids Surf. B: Biointerfaces 188 (2020), 110826, https://doi.org/10.1016/j.colsurfb.2020.110826.

[28] R.M. Rasal, A.V. Janorkar, D.E. Hirt, Poly(lactic acid) modifications, Prog. Polym. Sci. (2010), https://doi.org/10.1016/j.progpolymsci.2009.12.003.

[29] K.H.J. Buschow, F.R. de Boer, Physics of Magnetism and Magnetic Materials, 1st ed, Springer, US, Boston, MA, 2003, https://doi.org/10.1007/b100503.

[30] S. Mandal, K. Arts, H.C.M. Knoops, J.A. Cuenca, G.M. Klemencic, O.A. Williams, Surface zeta potential and diamond growth on gallium oxide single crystal, Carbon N. Y. 181 (2021) 79–86, https://doi.org/10.1016/j.carbon.2021.04.100.

[31] R. Egli, Magnetic susceptibility measurements as a function of temeperature and freqeuncy I: inversion theory, Geophys. J. Int. 177 (2009) 395–420, https://doi.org/10.1111/j.1365-246X.2009.04081.x.

[32] S.R. Gorodkin, R.O. James, W.I. Kordonski, Magnetic properties of carbonyl iron particles in magnetorheological fluids, J. Phys. Conf. Ser. 149 (2009), 012051, https://doi.org/10.1088/1742-6596/149/1/012051.

[33] L. Maldonado-Camargo, M. Unni, C. Rinaldi, Magnetic characterization of iron oxide nanoparticles for biomedical applications, in, Methods Mol. Biol. (2017) 47–71, https://doi.org/10.1007/978-1-4939-6840-4_4.

[34] H. Ma, P. Tian, J. Pello, P.M. Bendix, L.B. Oddershede, Heat generation by irradiated complex composite nanostructures, ACS Nano Lett. 14 (2014) 612–619, https://doi.org/10.1021/nl403798j.

[35] P.V. Ruijgrok, N.R. Verhart, P. Zijlstra, A.L. Tchebotareva, M. Orrit, Brownian fluctuations and heating of an optically aligned gold nanorod, Phys. Rev. Lett. 107 (2011) 1–4, https://doi.org/10.1103/PhysRevLett.107.037401.

[36] A. Kyrsting, P.M. Bendix, D.G. Stamou, L.B. Oddershede, Heat profiling of three-dimensionally optically trapped gold, Nano Lett. 11 (2011) 888–892, https://doi.org/10.1021/nl104280c.

[37] L. Jauffred, S.M.R. Taheri, R. Schmitt, H. Linke, L.B. Oddershede, Optical trapping of gold nanoparticles in air, Nano Lett. 15 (2015) 4713–4719, https://doi.org/10.1021/acs.nanolett.5b01562.

[38] M. Gai, J. Frueh, T. Tao, A.V. Petrov, V.V. Petrov, E.V. Shesterikov, S. I. Tverdokhlebov, G.B. Sukhorukov, Polylactic acid nano- and microchamber arrays for encapsulation of small hydrophilic molecules featuring drug release *via* high intensity focused ultrasound, Nanoscale. 9 (2017) 7063–7070, https://doi.org/10.1039/C7NR01841J.

[39] B.G. De Geest, S. De Koker, K. Immesoete, J. Demeester, S.C. De Smedt, W. E. Hennink, Self-exploding beads releasing microcarriers, Adv. Mater. 20 (2008) 3687–3691, https://doi.org/10.1002/adma.200800907.